

## Removal of orange G via environmentally friendly GO@Fe<sub>3</sub>O<sub>4</sub>-COOH@NH<sub>2</sub>-MIL-101(Fe) nanocomposite

Hui Huang<sup>a</sup>, Bin Huang<sup>a</sup>, Yichun Huang<sup>a</sup>, Jinbei Yang<sup>a,b,\*</sup>, Yinnv Ye<sup>a</sup>, Yucheng Chen<sup>a,b</sup>

<sup>a</sup>School of Ocean Science and Biochemistry Engineering, Fuqing Branch of Fujian Normal University, Fuzhou 350300, Fujian, China, emails: yangjinbei@sina.com (J. Yang), 28167724@qq.com (H. Huang), 1486210151@qq.com (B. Huang), 1971295040@qq.com (Y. Huang), 1901355863@qq.com (Y. Ye), 916115417@qq.com (Y. Chen)

<sup>b</sup>Fujian Provincial Key Laboratory of Coastal Basin Environment, Fujian Polytechnic Normal University, Fuzhou 350300, China

Received 24 January 2021; Accepted 15 April 2021

### ABSTRACT

Attractive environmentally friendly magnetic metal-organic framework (MOF) nanocomposite GO@Fe<sub>3</sub>O<sub>4</sub>-COOH@NH<sub>2</sub>-MIL-101(Fe) was synthesized by a solvothermal method and characterized by X-ray diffraction, Fourier transform infrared, scanning electron microscopy, Brunauer–Emmett–Teller, and vibrating sample magnetometer, and used as an effective adsorbent for the removal of orange G from aqueous solution. The various operating parameters that effect the adsorption process, such as adsorbent dosage (0.01–0.2 g), pH (1.0–10.0), initial concentration (50–400 mg L<sup>-1</sup>), and temperature (298.15–318.15 K) were studied. The percent removal of orange G increases with the increment of the adsorbent dosage and decrease of the initial concentration, and the optimum pH is 6.0. The Redlich–Peterson model can be favorably applied to describe the adsorption equilibrium data, indicating that the surfaces of GO@Fe<sub>3</sub>O<sub>4</sub>-COOH@NH<sub>2</sub>-MIL-101(Fe) nanocomposite for the orange G adsorption are made up of homogeneous adsorption patches. The adsorption kinetics indicate that the adsorption process of GO@Fe<sub>3</sub>O<sub>4</sub>-COOH@NH<sub>2</sub>-MIL-101(Fe) toward orange G obeys the pseudo-second-order model and the activation energy is 16.5 kJ mol<sup>-1</sup>. Thermodynamic parameters,  $\Delta H = 39.81$  kJ mol<sup>-1</sup>,  $\Delta S = -46.80$  J mol<sup>-1</sup> K<sup>-1</sup>, and  $\Delta G < 0$ , exhibit that the adsorption is exothermic and spontaneous. The maximum adsorption capacity of orange G onto GO@Fe<sub>3</sub>O<sub>4</sub>-COOH@NH<sub>2</sub>-MIL-101(Fe) nanocomposite is 128.8 mg g<sup>-1</sup>. Therefore, magnetic GO@Fe<sub>3</sub>O<sub>4</sub>-COOH@NH<sub>2</sub>-MIL-101(Fe) nanocomposite can be employed as an environmentally friendly and efficient adsorbent for the orange G removal from wastewater.

**Keywords:** Orange G; Adsorption; GO@Fe<sub>3</sub>O<sub>4</sub>-COOH@MIL-101(Fe); Kinetic; Thermodynamics

### 1. Introduction

Organic dyes are extensively used in the printing, leather, paper, and textile industries. A large amount of industrial wastewater containing organic dye is produced every year, which can lead to serious pollution to the ecological environment and water sources, cause serious diseases and endanger human life and health. Orange G is a typical anionic azo dye, which is a kind of organic compound with aryl groups at both ends of the azo group.

Its structure is exhibited in Fig. 1. The list of carcinogens published by the International Agency for Research on Cancer of the World Health Organization was preliminarily sorted out in 2017. Orange G is included in the list of three carcinogens due to its acute toxicity and mutagenicity, which has some chromosomal damage and clastogenic activity as special toxic effects [1,2]. The decomposition of orange G at high temperatures will promote the release of harmful gases, such as carbon dioxide, sulfur oxides, sodium oxide, and nitrogen oxides, which will aggravate

\* Corresponding author.

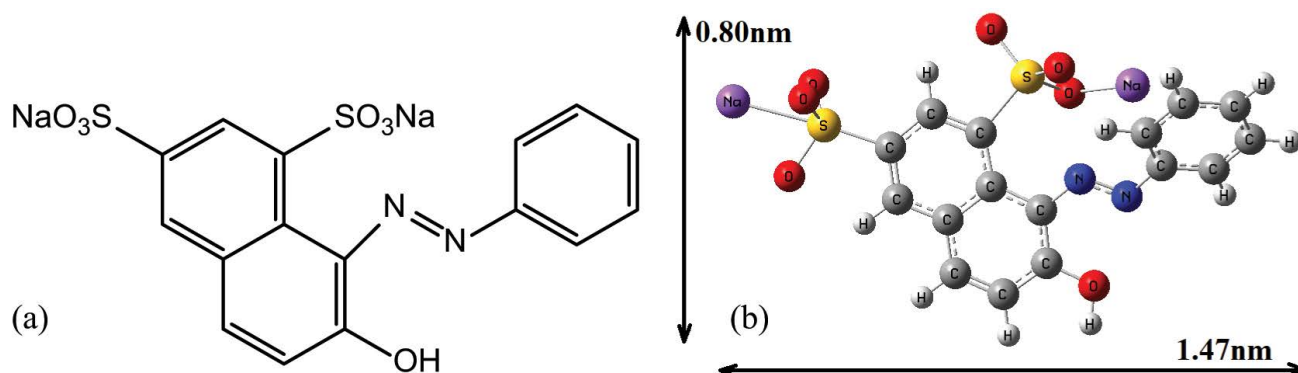


Fig. 1. Chemical structure (a) and molecular structure (b) of orange G.

environmental phenomena such as global warming and acid rain [3]. Hence, the removal of orange G pollutants from the effluent is highly significant for water safety and human health.

Nowadays, many technologies have been used for the elimination of dyes from wastewater, such as chemical oxidation [4,5], electrochemical treatment [6,7], membrane separation [8,9], photodegradation [10,11], biological treatment [12,13], and adsorption [14–21]. Among the above technologies, adsorption is considered as the most competitive method, due to its high efficiency, low cost, recyclability, and easy operation [22]. Various types of adsorbents have been reported for dye removal, such as activated carbon [23–25], agricultural waste [26,27], industry solid waste [28,29], graphene [30], clay minerals [31,32], halloysite [33], etc. These low-cost friendly adsorbents have been widely used, but there are still some shortcomings, such as limited adsorption capacity. Therefore, there is still a need to develop new adsorbents with excellent adsorption capacity and high selectivity.

Metal organic framework (MOF) is a type of crystalline material composed of coordination bonds between transition metal cations and multidentate organic linkers [34,35]. The structure of MOF is characterized by being porous (porous material) open frame, which is regarded as an environmentally friendly material to remove dye in water because of the high surface area and excellent stability [36]. Arora et al. [37] developed Fe-BDC MOF for the removal of the toxic dye methylene blue from industrial waste. By increasing the dose of adsorbent and temperature, 94.74% of the dye can be removed. Soni et al. [38] attempted to improve the adsorption performance of Fe-Benzene dicarboxylic acid MOF to remove methylene blue dye from wastewater through cobalt doping. The removal efficiency of Co-doped Fe-BDC MOF increased from 8.56 to 23.92 mg g<sup>-1</sup>. Graphene oxide (GO) is also considered as a potential environmental cleaning adsorbent through the combination of electrostatic attraction,  $\pi$ - $\pi$  stacking, and hydrogen bonding interactions because of its attractive properties and high removal efficiency of water pollutants [39]. Whereas the low separation efficiency of MOF or GO from aqueous solutions still limits its industrial application. So far, how to simultaneously utilize the adsorption properties of MOF/GO and the development

of effective methods to overcome the separation problem remains a challenge. In recent years, magnetic separation technology has become an emerging technology in the field of wastewater treatment. The combination of MOF, GO, and magnetic nanoparticles to prepare MOF/GO-based composites realizes solid-liquid separation. Thus, in the present work, a GO@Fe<sub>3</sub>O<sub>4</sub>-COOH@NH<sub>2</sub>-MIL-101(Fe) nanocomposite was synthesized via solvothermal method and characterized by X-ray diffraction (XRD), Fourier transform infrared (FT-IR), scanning electron microscopy (SEM), Brunauer–Emmett–Teller (BET), and vibrating sample magnetometer (VSM). Orange G was selected as the representative of anionic azo dyes to study the adsorption behavior of the obtained composite. The effect of adsorbent dosage, solution pH, initial concentration, and temperature on the adsorption performance was evaluated. Furthermore, the adsorption isotherms, thermodynamics, and kinetics of orange G on the nanocomposite were also carried out.

## 2. Experimental

### 2.1. Materials

Ferric chloride, ferrous chloride, oleic acid, *N,N*-dimethylformamide, 2-aminoterephthalic acid, ethanol, graphene oxide (GO), and orange G (C<sub>16</sub>H<sub>10</sub>N<sub>2</sub>Na<sub>2</sub>O<sub>7</sub>S<sub>2</sub>) were purchased from Shanghai Aladdin (Shanghai, China). Ammonia, acetic acid, hydrochloric acid, potassium permanganate, sodium nitrate, sulfuric acid, and hydrogen peroxide were obtained from Sinopharm Chemical Reagent (Shanghai, China). More information about the used materials is shown in Table 1.

### 2.2. Methods

#### 2.2.1. Analysis method

The orange G concentration was determined by a visible spectrophotometer (UV-1800PC, Shanghai MAPADA Instrument Co., Ltd., China) at 665 nm. The standard curve of the orange G concentration ( $y$ , mg L<sup>-1</sup>) vs. absorbance ( $x$ ) is  $y = 41.4518x - 0.1083$ , the range of  $x$  is 0–25.0, and the determination coefficients of the curve are 0.9998.

Table 1  
Chemical sample description

Chemicals	Source	Purity	Molecular weight	CAS number
Ferric chloride	Shanghai Aladdin	≥99.9%	162.20	7705-08-0
Ferrous chloride	Shanghai Aladdin	≥99.5%	126.75	7758-94-3
Oleic acid	Shanghai Aladdin	≥99.0%	282.46	112-80-1
<i>N,N</i> -dimethylformamide	Shanghai Aladdin	≥99.9%	73.09	68-12-2
2-aminoterephthalic acid	Shanghai Aladdin	≥98.0%	181.15	10312-55-7
Ethanol	Shanghai Aladdin	≥99.5%	46.07	64-17-5
Graphene oxide	Shanghai Aladdin	≥99.0%	12.01	7782-42-5
Orange G	Shanghai Aladdin	≥96.0%	452.37	1936-15-8
Ammonia	Sinopharm Chemical	28%	17.03	7664-41-7
Acetic acid	Sinopharm Chemical	≥99.8%	60.05	64-19-7
Hydrochloric acid	Sinopharm Chemical	36%	36.46	7647-01-0
Potassium permanganate	Sinopharm Chemical	≥99.5%	158.03	7722-64-7
Sodium nitrate	Sinopharm Chemical	≥99.0%	84.99	7631-99-4
Sulfuric acid	Sinopharm Chemical	≥96.0%	98.08	7664-93-9
Hydrogen peroxide	Sinopharm Chemical	30%	34.01	7722-84-1

### 2.2.2. Preparation of $\text{Fe}_3\text{O}_4\text{-COOH}$

0.03 mol of  $\text{FeCl}_3 \cdot 6\text{H}_2\text{O}$  was dissolved in 145 mL of deionized water in a 250 mL three-necked flask with a stirring speed of 200 rpm at 70°C. 0.02 mol of  $\text{FeCl}_2 \cdot 4\text{H}_2\text{O}$  were dissolved in 10 mL of deionized water, and 7.5 mL filtrate was added into the above three-necked flask after filtration. Subsequently, 20 mL of 25% ammonia was added dropwise under vigorous stirring. After 1 min, 0.015 mol of oleic acid was dropped into the three-necked flask and the mixture continues to react at 70°C for 1 h. After the reaction, a black sol-like substance was obtained, and the precipitate was separated from the mixture by an external magnet. The precipitate was washed twice with ethanol to remove excess oleic acid and several times with deionized water until the pH of the filtrate was neutral. The obtained precipitate was mixed with 160 mL of 10 mg mL<sup>-1</sup>  $\text{KMnO}_4$  solutions, and then the mixed liquid was sonicated for 8 h. After magnetic separation, the magnetic  $\text{Fe}_3\text{O}_4\text{-COOH}$  solid was washed several times with distilled water and thereby dried at 90°C for 12 h. The dried  $\text{Fe}_3\text{O}_4\text{-COOH}$  solid was then cooled, ground, and sieved through a 100-mesh screen, and stored in a desiccator.

### 2.2.3. Preparation of $\text{Fe}_3\text{O}_4\text{-COOH@NH}_2\text{-MIL-101(Fe)}$ nanocomposite

$\text{Fe}_3\text{O}_4\text{-COOH@MIL-101(Fe)}$  nanocomposite was synthesized by a solvothermal method as follows: 0.001 mol  $\text{Fe}_3\text{O}_4\text{-COOH}$ , 0.0032 mol  $\text{FeCl}_3 \cdot 6\text{H}_2\text{O}$ , 0.0032 mol 2-aminoterephthalic acid, 0.0509 mol acetic acid, and 0.9393 mol *N,N*-dimethylformamide were added sequentially into a 100 mL conical flask. The mixture was sonicated for 30 min. Then, the dissolved sample was sent to a stainless-steel reactor and crystallized at 110°C for 24 h. After cooling to room temperature, the brown powder was obtained by centrifugation and washed twice with *N,N*-dimethylformamide, and ethanol for 30 min. After washing,

the desired nanocomposite was dried at 90°C for 12 h in a vacuum oven. The dried product was then cooled, ground, and sieved through a 100-mesh screen, and stored in desiccators for use.

### 2.2.4. Preparation of $\text{GO@Fe}_3\text{O}_4\text{-COOH@NH}_2\text{-MIL-101(Fe)}$ nanocomposite

The preparation method of  $\text{GO@Fe}_3\text{O}_4\text{-COOH@NH}_2\text{-MIL-101(Fe)}$  nanocomposite was the same as that in section 2.2.3 (Preparation of  $\text{Fe}_3\text{O}_4\text{-COOH@NH}_2\text{-MIL-101(Fe)}$  nanocomposite), except that 5% graphene oxide was added in the first step of the synthesis.

### 2.3. Characterization

The phase and crystal structure of the sample was measured by XRD spectroscopy (Rigaku UltimaIV, Japan) using  $\text{Cu K}\alpha$  radiation. The FT-IR spectra of the sample were determined by a Nicolet iS10 infrared spectrometer of Thermo Fisher Co., (USA) using the KBr pellet in the frequency range of 4,000–400 cm<sup>-1</sup>. The morphology of the sample was observed by SEM using a Hitachi SU8010 SEM (Japan).  $\text{N}_2$  adsorption–desorption isotherms and the pore size distribution of the sample were performed by an automatic surface analyzer (Micromeritics ASAP 2460, USA). The hysteresis loops were determined by an MPMS-7 VSM (Quantum Design, USA) to investigate the magnetic property of the samples at room temperature.

### 2.4. Adsorption experiments

The batch adsorption experiments were studied by adding different mass of the synthesized nanocomposite with 50 mL of orange G aqueous solution at the specified concentration and pH in a 100 mL flask. The solution was adjusted to the required pH value with 0.1 M HCl or NaOH. The flask

was then placed in a water bath oscillator and shaken at 210 rpm and constant temperature. The samples were taken and the concentration of orange G were determined through a visible spectrophotometer. The adsorption capacity of orange G on the synthesized nanocomposite at a given time ( $q_t$ , mg g<sup>-1</sup>) and at the state of equilibrium ( $q_e$ , mg g<sup>-1</sup>), and the percentage removal of orange G,  $R_e$  (%), were calculated as follows:

$$q_t = \frac{(C_0 - C_t)V}{m} \quad (1)$$

$$q_e = \frac{(C_0 - C_e)V}{m} \quad (2)$$

$$R_e(\%) = \frac{(C_0 - C_e)}{C_0} \times 100 \quad (3)$$

where  $m$  is the adsorbent mass (g),  $V$  is the volume of solution (L),  $C_0$  and  $C_t$  is the concentration at initial and specific time, respectively (mg L<sup>-1</sup>), and  $C_e$  is the concentration at equilibrium (mg L<sup>-1</sup>).

### 3. Results and discussion

#### 3.1. Characterization of the adsorbents

##### 3.1.1. X-ray diffraction

The powder XRD spectrum of Fe<sub>3</sub>O<sub>4</sub>-COOH, Fe<sub>3</sub>O<sub>4</sub>-COOH@NH<sub>2</sub>-MIL-101(Fe), and GO@Fe<sub>3</sub>O<sub>4</sub>-COOH@NH<sub>2</sub>-MIL-101(Fe) are exhibited in Fig. 2. The characteristic peaks of Fe<sub>3</sub>O<sub>4</sub>-COOH at 30.1°, 35.5°, 43.3°, 53.6°, 57.2°, and 62.3° are corresponding to the (220), (311), (400), (422), (511), and (440) of the crystal planes, respectively,

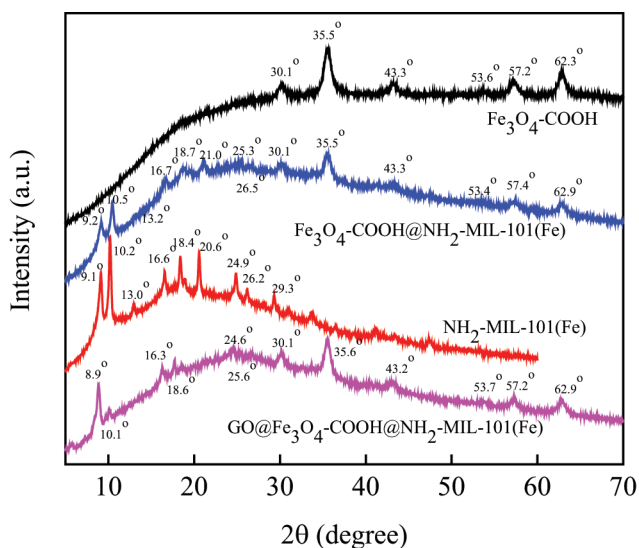


Fig. 2. XRD patterns of Fe<sub>3</sub>O<sub>4</sub>-COOH, NH<sub>2</sub>-MIL-101(Fe), Fe<sub>3</sub>O<sub>4</sub>-COOH@NH<sub>2</sub>-MIL-101(Fe), and GO@Fe<sub>3</sub>O<sub>4</sub>-COOH@NH<sub>2</sub>-MIL-101(Fe).

which indicates the cubic spinel structure of the magnetite. Low-angle (<30°) XRD patterns of Fe<sub>3</sub>O<sub>4</sub>-COOH@NH<sub>2</sub>-MIL-101(Fe) and GO@Fe<sub>3</sub>O<sub>4</sub>-COOH@NH<sub>2</sub>-MIL-101(Fe) nanocomposite were in agreement with the synthesized NH<sub>2</sub>-MIL-101(Fe). Except for the diffraction peaks of NH<sub>2</sub>-MIL-101(Fe), six new diffraction peaks of Fe<sub>3</sub>O<sub>4</sub>-COOH were also observed in the XRD patterns of Fe<sub>3</sub>O<sub>4</sub>-COOH@NH<sub>2</sub>-MIL-101(Fe) and GO@Fe<sub>3</sub>O<sub>4</sub>-COOH@NH<sub>2</sub>-MIL-101(Fe) nanocomposite. After the introduction of GO, the XRD spectrum of GO@Fe<sub>3</sub>O<sub>4</sub>-COOH@NH<sub>2</sub>-MIL-101(Fe) nanocomposite remained basically unchanged, and the diffraction peak did not significantly shift, which shows that the introduction of GO doesn't change the skeleton structure of NH<sub>2</sub>-MIL-101(Fe).

##### 3.1.2. Fourier transform infrared

The FT-IR spectrum of Fe<sub>3</sub>O<sub>4</sub>-COOH, GO, Fe<sub>3</sub>O<sub>4</sub>-COOH@NH<sub>2</sub>-MIL-101(Fe), and GO@Fe<sub>3</sub>O<sub>4</sub>-COOH@NH<sub>2</sub>-MIL-101(Fe) before and after adsorption depicted in Fig. 3. For Fe<sub>3</sub>O<sub>4</sub>-COOH, the characteristic peak was observed at 580 cm<sup>-1</sup>, which was associated with the typical Fe–O vibration [40]. The strong characteristic peaks at 3,423 and 1,633 cm<sup>-1</sup> corresponds to the strong stretching vibrations of the hydroxyl and carboxyl groups, respectively. For GO, the characteristic peak at 1,732 cm<sup>-1</sup> is related to the stretching vibration of C=O of the carboxyl group. The vibration at 1,400 cm<sup>-1</sup> corresponds to the stretching vibration of C–OH on the surface of GO. The vibration at 1,630 cm<sup>-1</sup> is attributed to the C=C double bond of the benzene-like ring skeleton structure. For Fe<sub>3</sub>O<sub>4</sub>-COOH@NH<sub>2</sub>-MIL-101(Fe) and GO@Fe<sub>3</sub>O<sub>4</sub>-COOH@NH<sub>2</sub>-MIL-101(Fe), the characteristics of the infrared spectrum mainly reflect the benzene carboxylate and amine groups: the band at 1,580 and 1,380 cm<sup>-1</sup> corresponded to the antisymmetric and symmetric stretching vibrations of the CO bonding in the carboxylates, and the characteristic peak at 1,260 cm<sup>-1</sup> is related to the aromatic

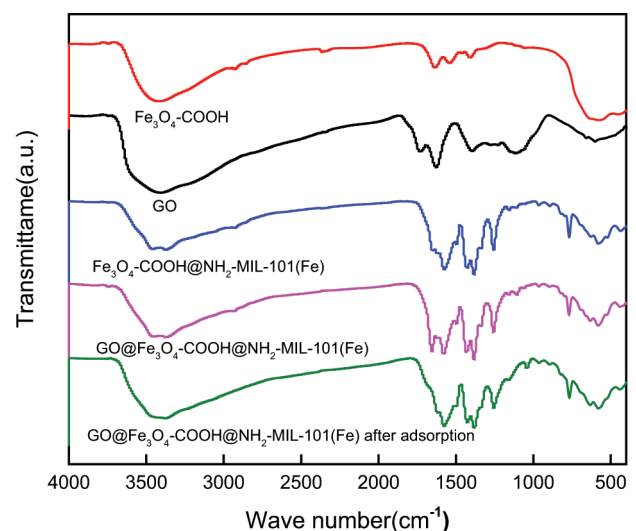


Fig. 3. FT-IR spectroscopy of Fe<sub>3</sub>O<sub>4</sub>-COOH, GO, Fe<sub>3</sub>O<sub>4</sub>-COOH@NH<sub>2</sub>-MIL-101(Fe), and GO@Fe<sub>3</sub>O<sub>4</sub>-COOH@NH<sub>2</sub>-MIL-101(Fe) before and after adsorption.

carbon C–N stretching mode. Furthermore, the appearance of double peaks at 3,460 and 3,370  $\text{cm}^{-1}$  were reflected by antisymmetric and symmetric stretching vibrations of the amine group. The characteristic peak at 768  $\text{cm}^{-1}$  is related to the Fe–OH group, showing a large number of surface-active sites generated by the dissociative adsorption of water. After adsorption, the IR spectrum of  $\text{GO@Fe}_3\text{O}_4\text{-COOH@NH}_2\text{-MIL-101(Fe)}$  remains almost unchanged.

### 3.1.3. Scanning electron microscopy

The morphology and structure of the as-prepared  $\text{Fe}_3\text{O}_4\text{-COOH@NH}_2\text{-MIL-101(Fe)}$  and  $\text{GO@Fe}_3\text{O}_4\text{-COOH@NH}_2\text{-MIL-101(Fe)}$  before and after adsorption, characterized by SEM, are exhibited in Fig. 4. The  $\text{Fe}_3\text{O}_4\text{-COOH}$  are approximately spherical (Fig. 4a). The SEM images of two  $\text{NH}_2\text{-MIL-101(Fe)}$  exhibit concave octahedral morphology, which are enclosed by  $\text{Fe}_3\text{O}_4\text{-COOH}$  or GO (Figs. 4b and c). The electrostatic interactions between the negatively charged  $\text{Fe}_3\text{O}_4\text{-COOH}$  (or GO) and positively charged  $\text{NH}_2\text{-MIL-101(Fe)}$  cause the magnetic  $\text{Fe}_3\text{O}_4\text{-COOH}$  or GO to be evenly dispersed on the surface of  $\text{NH}_2\text{-MIL-101(Fe)}$ . After adsorption, the structure of  $\text{GO@Fe}_3\text{O}_4\text{-COOH@NH}_2\text{-MIL-101(Fe)}$  doesn't collapse but remains almost unchanged, exhibited its good stability.

### 3.1.4. Nitrogen adsorption–desorption

The surface area and pore volume of the obtained materials evaluated by  $\text{N}_2$  adsorption/desorption are exhibited in Fig. 5. The nitrogen adsorption/desorption isotherms of the two MOFs materials are of type IV with a hysteresis loop at high relative pressures, which is the characteristic of mesoporous features (2–50 nm) [41]. The BET surface areas of  $\text{Fe}_3\text{O}_4\text{-COOH}$ ,  $\text{Fe}_3\text{O}_4\text{-COOH@NH}_2\text{-MIL-101(Fe)}$ , and  $\text{GO@Fe}_3\text{O}_4\text{-COOH@NH}_2\text{-MIL-101(Fe)}$  are 99.49, 147.91, and 358.02  $\text{m}^2 \text{g}^{-1}$ , respectively. The total pore volumes of them are 0.3445, 0.4202, and 0.4865  $\text{m}^3 \text{g}^{-1}$ , respectively. The pore sizes of them are 13.85, 11.36, and 5.43 nm, respectively. Compared with the parent MOF structure reported in the literature [42,43], the texture parameter size decreased significantly, which may be due to the high dispersion of  $\text{Fe}_3\text{O}_4\text{-COOH}$  or GO on the pores of  $\text{NH}_2\text{-MIL-101(Fe)}$ .

### 3.1.5. Magnetization

The magnetization curves of  $\text{Fe}_3\text{O}_4\text{-COOH}$  and  $\text{GO@Fe}_3\text{O}_4\text{-COOH@NH}_2\text{-MIL-101(Fe)}$  are displayed in Fig. 6. The plots indicate that the nanocomposite exhibits typical superparamagnetic behavior. The saturation magnetization value for  $\text{GO@Fe}_3\text{O}_4\text{-COOH@NH}_2\text{-MIL-101(Fe)}$  is 13.5  $\text{emu g}^{-1}$ ,

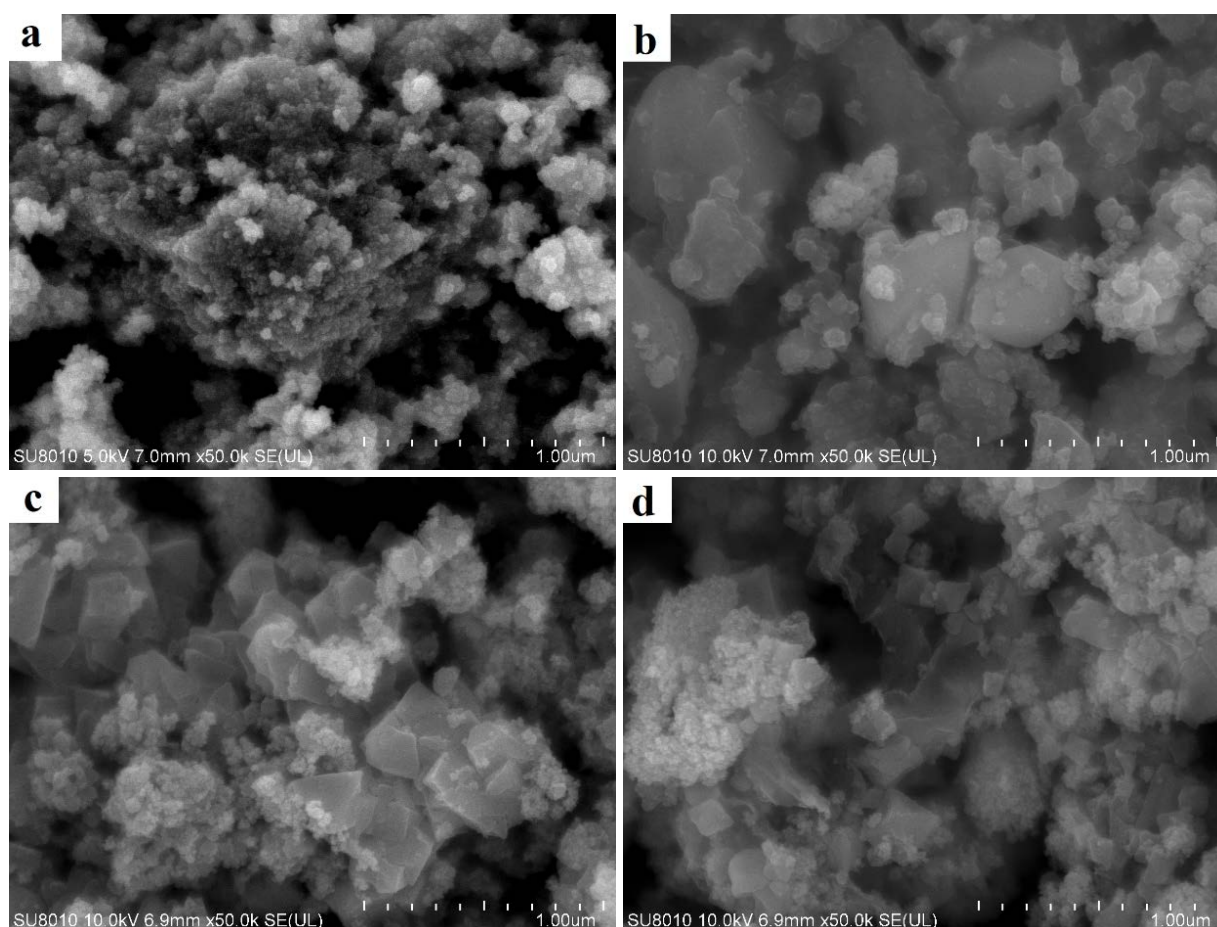


Fig. 4. SEM images of (a)  $\text{Fe}_3\text{O}_4\text{-COOH}$ , (b)  $\text{Fe}_3\text{O}_4\text{-COOH@NH}_2\text{-MIL-101(Fe)}$ , (c and d)  $\text{GO@Fe}_3\text{O}_4\text{-COOH@NH}_2\text{-MIL-101(Fe)}$  before and after adsorption.

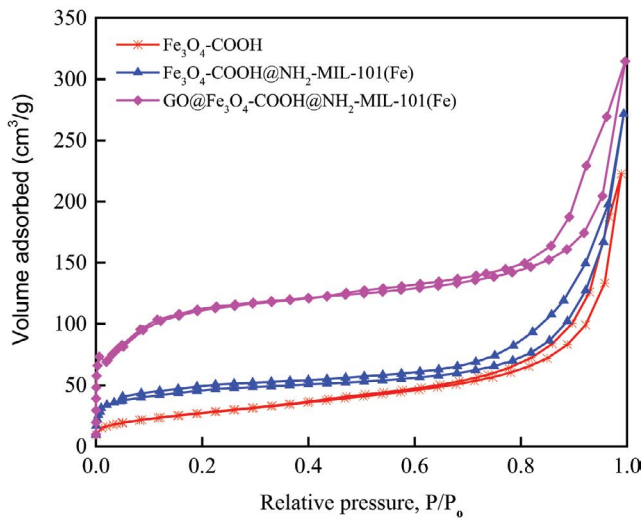


Fig. 5.  $N_2$  adsorption and desorption isotherm of  $Fe_3O_4$ -COOH,  $Fe_3O_4$ -COOH@ $NH_2$ -MIL-101(Fe), and  $GO@Fe_3O_4$ -COOH@ $NH_2$ -MIL-101(Fe).

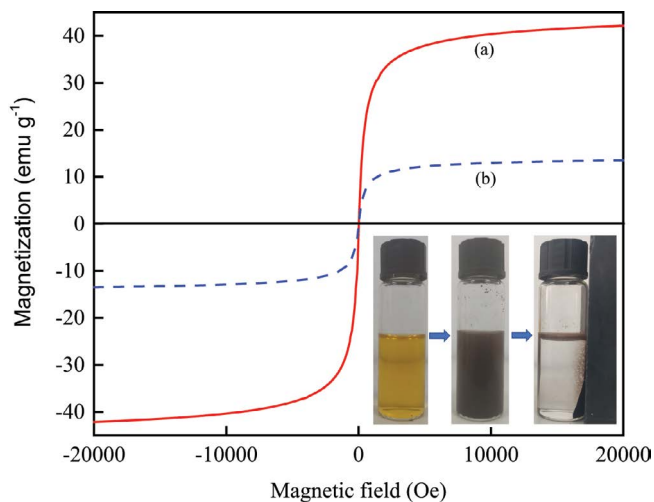


Fig. 6. Magnetization curve of (a)  $Fe_3O_4$ -COOH and (b)  $GO@Fe_3O_4$ -COOH@ $NH_2$ -MIL-101(Fe) at room temperature. The inset displays the photographs of the dyes solution (left) adsorption system before (middle) and after (right) magnetic separation.

which is sufficient for magnetic separation with a conventional magnet. The superparamagnetic behavior is mainly generated by the magnetite  $Fe_3O_4$ -COOH in the nanocomposite, whose saturation magnetization is  $42.1 \text{ emu g}^{-1}$ . The inset in Fig. 6 exhibits the adsorption process of orange G onto  $GO@Fe_3O_4$ -COOH@ $NH_2$ -MIL-101(Fe).  $GO@Fe_3O_4$ -COOH@ $NH_2$ -MIL-101(Fe) has good dispersibility after shaking and can be easily separated from the dye solution within a few minutes by magnetic separation. At the same time, the color of the dye solution also obviously disappeared. The above phenomena indicate that the nanocomposite has adsorption capacity and magnetism.

### 3.2. Factors affecting adsorption

#### 3.2.1. Effect of different adsorbents

The effect of different adsorbents on orange G removal was carried out by taking 50 mL of  $50 \text{ mg L}^{-1}$  orange G solution containing 0.04 g adsorbent shaken at 210 rpm and 298.15 K for 5 h. The equilibrium adsorption capacity of orange G by different adsorbents was determined and is displayed in Fig. 7a. As shown in this figure, the sequence of the equilibrium adsorption capacity of orange G on the four adsorbents is  $GO@Fe_3O_4$ -COOH@ $NH_2$ -MIL-101(Fe) >  $Fe_3O_4$ -COOH@ $NH_2$ -MIL-101(Fe) > GO >  $Fe_3O_4$ -COOH, and the values are 42.93, 35.45, 13.95, and  $7.61 \text{ mg g}^{-1}$ , respectively.  $GO@Fe_3O_4$ -COOH@ $NH_2$ -MIL-101(Fe) has the maximum adsorption capacity in the four adsorbents for orange G, which was selected to remove orange G from the aqueous solution in the further work.

#### 3.2.2. Effect of adsorbent dosage

The effect of adsorbent dosage (0.01–0.2 g) of  $GO@Fe_3O_4$ -COOH@ $NH_2$ -MIL-101(Fe) nanocomposite on the removal of orange G was investigated by mixing different dosage of adsorbent with 50 mL of orange G solutions of  $50 \text{ mg L}^{-1}$  at 210 rpm and 298.15 K for 5 h. The equilibrium adsorption capacity and the percent removal of orange G were obtained, and the results are exhibited in Fig. 7b. As displayed in Fig. 7b, the percent removal of orange G is promoted with increasing mass of adsorbent due to the more active sites for adsorption. Whereas, the percent removal tends to be consistently near to 95.82% when the adsorbent dosage is beyond 0.04 g. The equilibrium adsorption capacity of orange G continues to decrease with the increase in the amount of adsorbent. This is due to the relatively high dye concentration and the effective utilization of the adsorption sites of the adsorbent at a lower adsorbent concentration. The  $GO@Fe_3O_4$ -COOH@ $NH_2$ -MIL-101(Fe) nanocomposite has a higher unit adsorption capacity for orange G. The decrease in unit adsorption capacity is due to the increase in adsorbent amount which reduces the concentration gradient between adsorbent and adsorbate [44]. In addition, the molecular structure and size of orange G were determined by the density functional theory (DFT) at b3lyp/6–31+g(d,p) level using Gaussian 16 program and displayed in Fig. 1. The size of orange G is smaller than the average pore size of the used adsorbent  $GO@Fe_3O_4$ -COOH@ $NH_2$ -MIL-101(Fe) nanocomposite, which shows that orange G molecules can enter the pores of the adsorbent and be adsorbed in the pores.

#### 3.2.3. Effect of pH

The pH of the solution is one of the key factors affecting the adsorption of dye on the adsorbent which can change the charge distribution on the surface of the adsorbent and speciation of adsorbate [45]. The effect of pH was studied in the pH range from 1.0 to 10.0 with 50 mL of  $50 \text{ mg L}^{-1}$  orange G solution and 0.04 g  $GO@Fe_3O_4$ -COOH@ $NH_2$ -MIL-101(Fe) nanocomposite at 210 rpm and 298.15 K for 5 h. The equilibrium adsorption capacity of orange G was determined and is presented in Fig. 7c. It is obvious that the removal

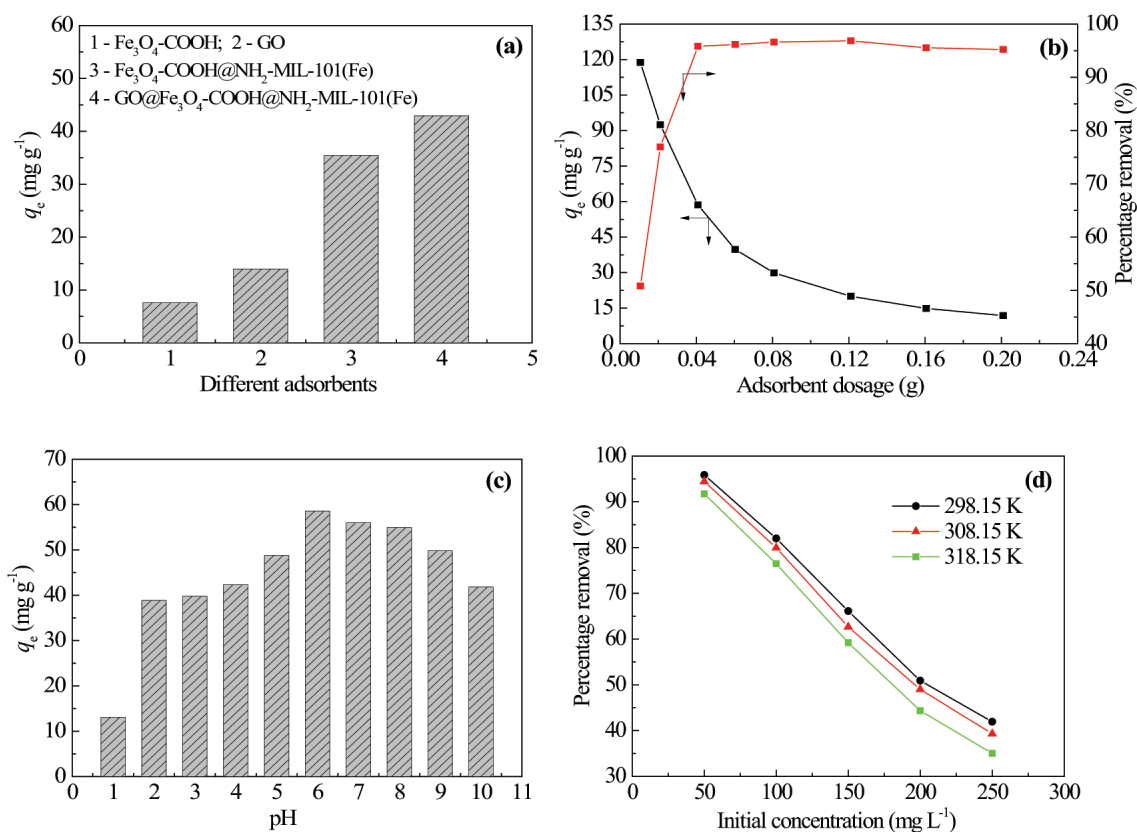


Fig. 7. Effect of (a) different adsorbents, (b) adsorbent dosage, (c) pH, and (d) initial concentration on the adsorption of orange G.

of orange G for  $\text{GO@Fe}_3\text{O}_4\text{-COOH@NH}_2\text{-MIL-101(Fe)}$  nanocomposite is highly pH-dependent. The equilibrium adsorption capacity increases rapidly from 13.08 to 58.57  $\text{mg g}^{-1}$  for an increase in pH from 1 to 6. Further, increase in the pH from 6 to 10 accompanied by a decrease in the adsorption capacity from 58.57 to 41.85  $\text{mg g}^{-1}$ . The maximum adsorption capacity occurs at pH 6.

The pH value not only affects the surface charge of the adsorbent and the charged state of the functional groups but also affects the state of the adsorbate, which makes each system have its corresponding optimal adsorption pH. The point-of-zero-charge of the  $\text{GO@Fe}_3\text{O}_4\text{-COOH@NH}_2\text{-MIL-101(Fe)}$  nanocomposite was determined and the value is 6.4, which indicates that the surface of the nanocomposite is positive below a pH of 6.4, and negative above a pH of 6.4. Meanwhile, the pKa values of orange G are 11.5 and 1.0 for the deprotonation of the naphthalene OH and the two  $\text{SO}_3\text{H}$  groups, respectively [46,47]. As the pH value varied from 1 to 6, the improved adsorption capacity of orange G was ascribed to existing strong electrostatic attraction forces between the positively charged surface of the  $\text{GO@Fe}_3\text{O}_4\text{-COOH@NH}_2\text{-MIL-101(Fe)}$  nanocomposite and the negatively charged orange G due to the deprotonation of the two  $\text{SO}_3\text{H}$  groups. The adsorption capacity of orange G decreases with increasing pH from 6 upto 10, due to the electrostatic repulsion between the negatively charged surface of the nanocomposite adsorbent and the orange G molecule, which inhibits the orange G removal. The above results indicate that one of the

absorption mechanisms could be the charge interactions between the adsorbent and orange G. Therefore, the pH was set at 6 in further studies.

### 3.2.4. Effect of initial concentration

The effect of initial concentration of orange G on the removal of orange G was investigated at different concentrations (50–400  $\text{mg L}^{-1}$ ) as follows:  $\text{GO@Fe}_3\text{O}_4\text{-COOH@NH}_2\text{-MIL-101(Fe)}$  nanocomposite, 0.04 g and 50 mL of orange G solution with different initial concentration were put into 100 mL flask. The mixture was shaken at 210 rpm and three different temperatures from 298.15 to 318.15 K for 5 h. The samples were analyzed and the equilibrium concentrations of orange G were calculated. The equilibrium adsorption capacity and the percentage removal of orange G were both determined and are displayed in Fig. 7d. As shown in the figure, the percentage removal of orange G gradually decreases with increasing the initial concentration from 50 to 400  $\text{mg L}^{-1}$ . The tendency can be attributed to the fact that sufficient active sites responsible for orange G removal are available at lower initial concentration and the interaction between the adsorbent and the orange G molecule is the strongest, thereby improving the removal efficiency. Moreover, at the same initial concentration, the percentage removal of orange G increase as the temperature decreases from 318.15 to 298.15 K, indicating that the increase in temperature is negative to adsorption, that is, the adsorption process is exothermic.

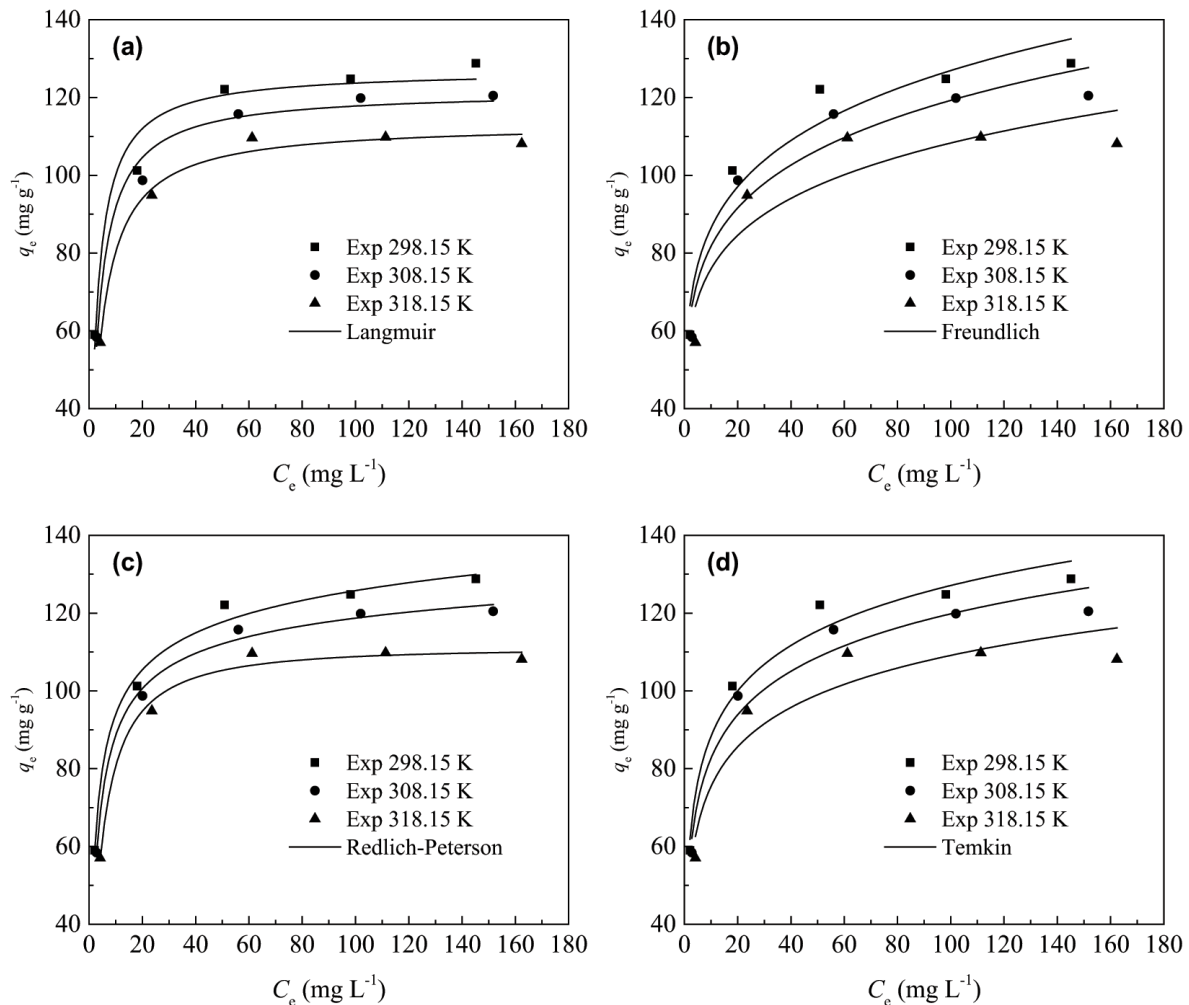


Fig. 8. Langmuir (a), Freundlich (b), Redlich–Peterson (c), and Temkin (d) isotherm plots for adsorption of orange G at different temperatures.

### 3.3. Adsorption isotherm

Adsorption isotherm is useful to describe the adsorption capacity and interactive behaviors between adsorbent and adsorbate. The adsorption isotherms of orange G on GO@Fe<sub>3</sub>O<sub>4</sub>-COOH@NH<sub>2</sub>-MIL-101(Fe) nanocomposite were carried out at temperatures of (298.15, 308.15, and 318.15 K). The detail condition was displayed in section 3.2.4 (Effect of initial concentration), and three adsorption equilibrium curves were shown in Fig. 8, which are the plots of  $q_e$  vs.  $C_e$ . In this work, the obtained adsorption data of orange G were analyzed by the widely used isotherms models, namely Langmuir (Eq. (4)), Freundlich (Eq. (5)), Redlich–Peterson (Eq. (6)), and Temkin (Eq. (7)) [48]. The non-linear forms of the selected models were shown as follows:

$$q_e = \frac{q_m K_L C_e}{1 + K_L C_e} \quad (4)$$

$$q_e = K_F C_e^{1/n_F} \quad (5)$$

$$q_e = \frac{K_{RP} C_e}{1 + \alpha_{RP} C_e} \quad (6)$$

$$q_e = \frac{RT}{\beta_T} \ln(\alpha_T \cdot C_e) \quad (7)$$

where  $T$  (K) and  $R$  (8.314 J mol<sup>-1</sup> K<sup>-1</sup>) are the absolute temperature and gas constant, respectively.  $q_m$  (mg g<sup>-1</sup>) is the maximum adsorption capacity and  $K_L$  (L mg<sup>-1</sup>) is the Langmuir equilibrium constant.  $n_F$  and  $K_F$  ((mg g<sup>-1</sup>)/mg L<sup>-1</sup>)<sup>1/n<sub>F</sub></sup> are the Freundlich constants.  $\alpha_{RP}$  ((L mg<sup>-1</sup>)<sup>0</sup>),  $K_{RP}$  (L g<sup>-1</sup>), and  $\theta$  ( $\leq 1$ ) are the Redlich–Peterson constants.  $\alpha_T$  (L mg<sup>-1</sup>) and  $\beta_T$  (J mol<sup>-1</sup>) are the Temkin constants.

The best-fit adsorption isotherm model was determined through non-linear method by judging the determination coefficient ( $R^2$ ) and the chi-square value ( $\chi^2$ ). The expression of the chi-square test was shown below [49,50]:

$$\chi^2 = \sum \frac{[(q_{e,\text{exp}} - q_{e,\text{cal}})]^2}{q_{e,\text{cal}}} \quad (8)$$

Table 2  
Isotherm parameters for the adsorption of Orange G

Models	Parameters	T (K)		
		298.15	308.15	318.15
Langmuir	$K_L$ (L mg <sup>-1</sup> )	0.3734	0.3062	0.2434
	$q_m$ (mg g <sup>-1</sup> )	127.01	121.66	113.35
	$R^2$	0.95217	0.97732	0.98662
	$\chi^2$	1.1840	0.4867	0.1936
Freundlich	$K_F$ ((mg g <sup>-1</sup> )/(mg L <sup>-1</sup> ) <sup>1/n<sub>F</sub></sup> )	6.0023	6.0972	6.5045
	$n_F$	58.92	56.06	53.33
	$R^2$	0.9171	0.8946	0.7969
	$\chi^2$	2.1925	2.3861	3.5444
Redlich-Peterson	$K_{RP}$ (L mg <sup>-1</sup> )	72.06	48.32	26.19
	$\alpha_{RP}$ ((L mg <sup>-1</sup> ) <sup>θ</sup> )	0.79	0.50	0.22
	$\theta$	0.93	0.95	1.01
	$R^2$	0.9841	0.9899	0.9812
	$\chi^2$	0.2351	0.1262	0.1872
Temkin	$\alpha_T$ (L mg <sup>-1</sup> )	19.06	16.90	17.58
	$\beta_T$ (J mol <sup>-1</sup> )	147.30	158.92	181.10
	$R^2$	0.9671	0.9510	0.8677
	$\chi^2$	0.7640	1.0092	2.1716

where the subscripts “exp” and “cal” correspond to the experimental and calculated values, respectively. It is not suitable to judge the best-fit adsorption isotherm only according to one parameter of the determination coefficient for the non-linear fitting. The chi-square analysis is a good method to find out the best-fit model [49]. If the value calculated from the model is in good agreement with the experimental data, the value of  $\chi^2$  will be little and near to zero, otherwise, there will be a huge deviation between the experiment and the model. The four non-linear forms of isotherms models were correlated to experimental data by Origin 2015 software and are exhibited in Fig. 8, and the obtained parameters are listed in Table 2. It can be seen from Table 2 that the maximal value of  $\chi^2$  and the minimal  $R^2$  at each temperature exhibits that the adsorption of orange G on GO@Fe<sub>3</sub>O<sub>4</sub>-COOH@NH<sub>2</sub>-MIL-101(Fe) nanocomposite is badly described by the Freundlich model. The Redlich–Peterson model is the best-fit isotherm model for the adsorption process due to the lowest values of  $\chi^2 \leq 0.23$  and the highest values of  $R^2 \geq 0.98$ .

The Redlich–Peterson model has the characteristics of both the Langmuir model and the Freundlich model, forming a hybrid adsorption mechanism, which can be used for multilayer and single-layer adsorption [51]. Furthermore, it can be used to depict the adsorption isotherm in a wide concentration range of adsorbate. The different values of parameter  $\theta$  represent that Redlich–Peterson model demonstrates different models: Langmuir ( $\theta \approx 1$ ), Freundlich ( $0 < \theta < 1$ ,  $K_{RP} \gg 1$ , and  $\alpha_{RP} \gg 1$ ), and Henry’s law ( $\theta = 0$ ). As displayed in Table 2, since the value of  $\theta$  is close to 1, the experimental data can be fitted better by the Langmuir isotherm than Freundlich at three different temperatures, indicating that the surfaces of GO@Fe<sub>3</sub>O<sub>4</sub>-COOH@NH<sub>2</sub>-MIL-101(Fe) nanocomposite for the orange G adsorption are made

up of homogeneous adsorption patches [52]. The maximum adsorption capacity of orange G onto GO@Fe<sub>3</sub>O<sub>4</sub>-COOH@NH<sub>2</sub>-MIL-101(Fe) nanocomposite acquired in the adsorption isotherms condition is 128.8 mg g<sup>-1</sup> at the orange G concentration of 250 mg L<sup>-1</sup> and 298.15 K.

### 3.4. Adsorption thermodynamics

The parameters of the adsorption thermodynamics of orange G by GO@Fe<sub>3</sub>O<sub>4</sub>-COOH@NH<sub>2</sub>-MIL-101(Fe) nanocomposite including the Gibbs free energy change ( $\Delta G$ ), the enthalpy change ( $\Delta H$ ), and the entropy change ( $\Delta S$ ) were calculated based on the following equations [53,54]:

$$\Delta G = -RT \ln K_e \tag{9}$$

$$\ln K_e = -\frac{\Delta H}{RT} + \frac{\Delta S}{R} \tag{10}$$

where  $K_e$  is the dimensionless thermodynamic equilibrium constant, and the value can be determined by converting the unit of the best-fit isotherm model Redlich–Peterson constant ( $K_{RP}$ ) [55]. The dimensionless  $K_e$  was calculated according to the following equation:

$$K_e = \frac{K_{RP} M_{\text{adsorbate}} [\text{Adsorbate}]^\theta}{\gamma} \tag{11}$$

where  $\gamma$  is the adsorbate activity coefficient,  $M_{\text{adsorbate}}$  (g mol<sup>-1</sup>) is the molar mass of adsorbate, and [Adsorbate] is the standard concentration of adsorbate (mol L<sup>-1</sup>). The molar mass of orange G is 452.37 g mol<sup>-1</sup>, and the activity coefficient and the standard concentration were set as 1 and 1 mol L<sup>-1</sup>, respectively.

The  $\Delta G$  values at different temperatures were calculated by Eq. (9). A straight line was obtained by plotting  $\ln K_e$  vs.  $1/T$ , which is displayed in Fig. 9, and the  $\Delta H$  and

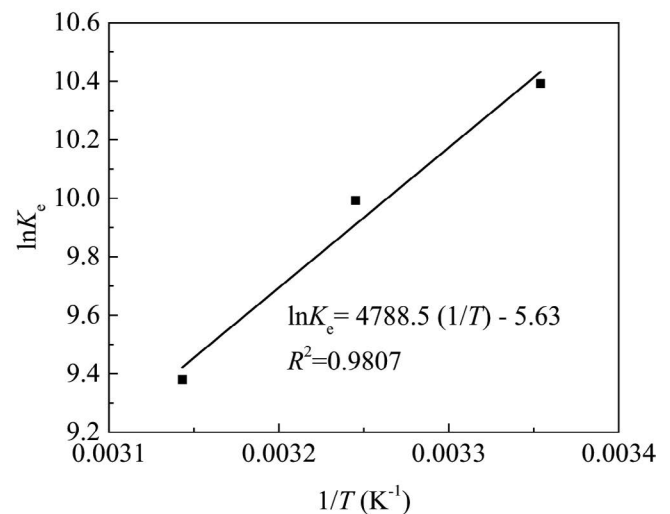


Fig. 9. Plot of  $\ln K_e$  vs.  $1/T$  for the thermodynamic parameters’ calculations.

$\Delta S$  values were determined from the slope and intercept of the straight line, respectively. The  $\Delta G$  values at three different temperatures of 298.15, 308.15, and 318.15 K are  $-25.76$ ,  $-25.60$ , and  $-24.81$  kJ mol $^{-1}$ , respectively. The negative values of  $\Delta G$  at three different temperatures exhibit the feasibility and spontaneity of the adsorption of orange

G on GO@Fe $_3$ O $_4$ -COOH@NH $_2$ -MIL-101(Fe) nanocomposite [56]. The negative value of  $\Delta S$  ( $-46.80$  J mol $^{-1}$  K $^{-1}$ ) reveals a decrease in the randomness at the adsorbate–solution interface [46]. Furthermore, the negative value of  $\Delta H$  ( $-39.81$  kJ mol $^{-1}$ ) confirms the exothermic nature of the adsorption process.

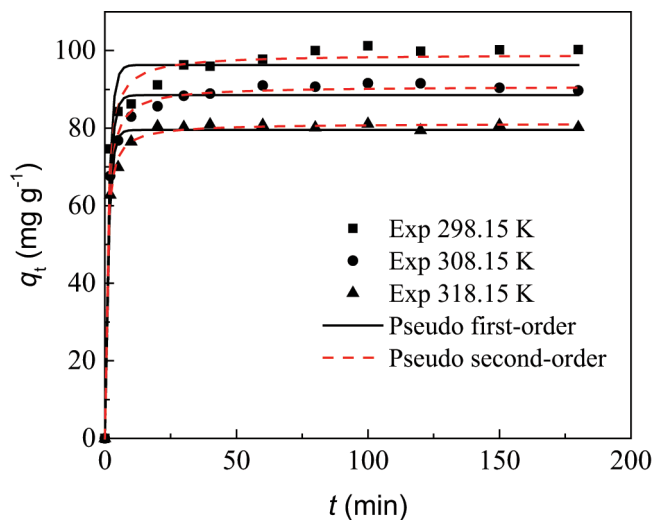


Fig. 10. Experimental data of adsorption kinetics and non-linear fitting of kinetics models.

Table 3  
Kinetic model parameters for the adsorption of Orange G

Models	Parameters	T (K)		
		298.15	308.15	318.15
Pseudo-first-order	$q_{e,exp}$ (mg g $^{-1}$ )	100.26	91.55	80.22
	$k_1$ (min $^{-1}$ )	0.6806	0.6547	0.7190
	$q_{e,cal}$ (mg g $^{-1}$ )	96.28	88.51	79.52
	$R^2$	0.9638	0.9779	0.9856
	$\chi^2$	3.1339	1.7769	1.0249
Pseudo-second-order	$k_2$ (g mg $^{-1}$ min $^{-1}$ )	0.0130	0.0145	0.0198
	$q_{e,cal}$ (mg g $^{-1}$ )	99.02	90.81	81.22
	$R^2$	0.9897	0.9971	0.9976
	$\chi^2$	0.9270	0.2418	0.1756

Table 4  
Comparison of adsorption capacity of various adsorbents for orange G

Adsorbents	Adsorption capacity (mg g $^{-1}$ )	Temperature (°C)	Reference
Formaldehyde modified Ragi Husk	14.1	25	[3]
Fe $_3$ O $_4$ @SiO $_2$ -MPS-g-DAC	109.1	45	[40]
Fe $_3$ O $_4$ /MIL-101 composite	200.0	25	[46]
Magnetic silica	61.3	25	[60]
Modified chitosan beads	63.7	25	[61]
Modified montmorillonite nanoclay	39.4	23	[62]
Prussian Blue nanoparticles	16.2	50	[63]
GO@Fe $_3$ O $_4$ -COOH@NH $_2$ -MIL-101(Fe)	128.8	25	This work

### 3.5. Adsorption kinetics

Adsorption kinetics is a significant characteristic to assess the efficiency of the adsorbent [57]. Moreover, the obtained kinetic parameters can also help to evaluate the adsorption rate and comprehend the mechanism of the adsorption process. The experiments of adsorption kinetics were studied as follows: 0.02 g of GO@Fe $_3$ O $_4$ -COOH@NH $_2$ -MIL-101(Fe) nanocomposite was mixed with 50 mL of 50 mg L $^{-1}$  orange G solution and put into a flask. The mixture was shaken at 210 rpm and the temperatures of (298.15, 308.15, and 318.15 K), respectively. The adsorption capacity of orange G on GO@Fe $_3$ O $_4$ -COOH@NH $_2$ -MIL-101(Fe) nanocomposite,  $q_t$  (mg g $^{-1}$ ) vs. time were calculated and are listed in Fig. 10. As displayed in Fig. 10, the adsorption rate and equilibrium adsorption capacity both improve with the decrease of temperature. The results further show that the adsorption of orange G on GO@Fe $_3$ O $_4$ -COOH@NH $_2$ -MIL-101(Fe) nanocomposite is exothermic, which is consistent with the thermodynamics of adsorption.

The adsorption kinetics data were fitted by pseudo-first-order (Eq. (12)) and pseudo-second-order (Eq. (13)) models [52,58]:

$$q_t = q_e [1 - \exp(-k_1 t)] \quad (12)$$

$$q_t = \frac{k_2 q_e^2 t}{1 + k_2 q_e t} \quad (13)$$

where  $k_1$  (min $^{-1}$ ) and  $k_2$  (g mg $^{-1}$  min $^{-1}$ ) are the rate constant of the pseudo-first-order and second-order models, respectively.

The adsorption kinetics data were correlated using the non-linear method by the determination coefficient ( $R^2$ ) and the chi-square value ( $\chi^2$ ) through Origin 2015 software, and the  $q_e$  in the chi-square ( $\chi^2$ ) of Eq. (9) was replaced by  $q_t$ . The correlating results are exhibited in Fig. 10 and the obtained kinetic parameters are listed in Table 3.

It can be seen from Fig. 10 and Table 3 that the values of  $R^2$  for the pseudo-second-order model are all higher than the pseudo-first-order model and the values of  $\chi^2$  for the pseudo-second-order model are all lower than the pseudo-first-order model. Furthermore, the experimental data of  $q_e$  ( $q_{e,exp}$ ) is more consistent with the calculated  $q_e$  ( $q_{e,cal}$ ) by the pseudo-second-order than the pseudo-first-order. Hence, the adsorption process of orange G on GO@Fe<sub>3</sub>O<sub>4</sub>-COOH@NH<sub>2</sub>-MIL-101(Fe) nanocomposite obeys the pseudo-second-order model instead of the pseudo-first-order model.

The adsorption activation energy was calculated by the logarithmic form of the Arrhenius equation as follows:

$$\ln k_2 = -\frac{E_a}{RT} + \ln A \quad (14)$$

where  $E_a$  (kJ mol<sup>-1</sup>) and  $A$  are the adsorption activation energy and frequency factor, respectively. A straight line was obtained by plotting  $\ln k_2$  vs.  $1/T$ , and the values of slope and intercept are -1,984.4 and 2.28, respectively. The determination coefficient  $R^2$  is 0.9185. The value of  $E_a$  was calculated from the slope of the plot as 16.5 kJ mol<sup>-1</sup>. Mostly, the activation energy of the chemical reaction is in the range from 42 to 420 kJ mol<sup>-1</sup> [59]. The value of  $E_a$  of orange G on GO@Fe<sub>3</sub>O<sub>4</sub>-COOH@NH<sub>2</sub>-MIL-101(Fe) nanocomposite is less than 42, which displays that the adsorption is a physical process.

### 3.6. Comparison with the reported adsorbents

For comparison, the performance of various adsorbents for the removal of orange G from aqueous solution are summarized in Table 4. It can be seen from Table 4 that the Fe<sub>3</sub>O<sub>4</sub>/MIL-101 composite displays the greatest adsorption capacity compared with the other adsorbents. It also shows that the maximum adsorption capacity of GO@Fe<sub>3</sub>O<sub>4</sub>-COOH@NH<sub>2</sub>-MIL-101(Fe) nanocomposite was higher than those reported for formaldehyde modified Ragi Husk, Fe<sub>3</sub>O<sub>4</sub>@SiO<sub>2</sub>-MPS-g-DAC, magnetic silica, modified chitosan beads, modified montmorillonite nanoclay, and Prussian Blue nanoparticles, which indicates that the adsorbent can be applied for new potential in adsorption system.

## 4. Conclusions

In the present work, two attractive magnetic MOF nanocomposites Fe<sub>3</sub>O<sub>4</sub>-COOH@NH<sub>2</sub>-MIL-101(Fe) and GO@Fe<sub>3</sub>O<sub>4</sub>-COOH@NH<sub>2</sub>-MIL-101(Fe) were synthesized by a solvothermal method and characterized by XRD, FT-IR, SEM, BET, and VSM, which were further used as adsorbent for the orange G removal from aqueous solution. GO@Fe<sub>3</sub>O<sub>4</sub>-COOH@NH<sub>2</sub>-MIL-101(Fe) has a higher adsorption capacity than Fe<sub>3</sub>O<sub>4</sub>-COOH@NH<sub>2</sub>-MIL-101(Fe). The % removal of orange G increases with the increment of the adsorbent dosage and decrease of the initial concentration, and the optimum pH is 6.0. The adsorption isotherm and kinetic data of orange G onto GO@Fe<sub>3</sub>O<sub>4</sub>-COOH@NH<sub>2</sub>-MIL-101(Fe) are best fitted by the Redlich–Peterson, and pseudo-second-order model models, respectively. The activation energy is 16.5 kJ mol<sup>-1</sup>. Thermodynamic parameters,  $\Delta H = 39.81$  kJ mol<sup>-1</sup>,

$\Delta S = -46.80$  J mol<sup>-1</sup> K<sup>-1</sup>, and  $\Delta G < 0$ , indicate that the adsorption process is exothermic and spontaneous. The maximum adsorption capacity of GO@Fe<sub>3</sub>O<sub>4</sub>-COOH@NH<sub>2</sub>-MIL-101(Fe) nanocomposite for orange G is 128.8 mg g<sup>-1</sup>. Hence, magnetic GO@Fe<sub>3</sub>O<sub>4</sub>-COOH@NH<sub>2</sub>-MIL-101(Fe) nanocomposite can be employed as an environmentally friendly adsorbent for the orange G removal from wastewater.

## Acknowledgments

We acknowledge the financial support for this work from the Natural Science Foundation of Fujian Province (No. 2019J05127), the Central Government Guides Local Science and Technology Development Project (2019L3013), and the China Scholarship Council (No. 201908350057).

## References

- [1] J.B. Tarkwa, N. Oturan, E. Acayanka, S. Laminsi, M.A. Oturan, Photo-Fenton oxidation of Orange G azo dye: process optimization and mineralization mechanism, *Environ. Chem. Lett.*, 17 (2019) 473–479.
- [2] M. Jyoti, Permissible synthetic food dyes in India, *J. Sci. Educ.*, 25 (2020) 567–577.
- [3] V.V. Dev, B. Wilson, K.K. Nair, S. Antony, K.A. Krishnan, Response surface modeling of Orange-G adsorption onto surface tuned ragi husk, *Colloid Interface Sci. Commun.*, 41 (2021) 100363, doi: 10.1016/j.colcom.2021.100363.
- [4] S. Sethi, B.S. Kaith, Saruchi, V. Kumar, Fabrication and characterization of microwave assisted carboxymethyl cellulose-gelatin silver nanoparticles imbided hydrogel: Its evaluation as dye degradation, *React. Funct. Polym.*, 142 (2019) 134–146.
- [5] P.K. Malik, S.K. Saha, Oxidation of direct dyes with hydrogen peroxide using ferrous ion as catalyst, *Sep. Purif. Technol.*, 31 (2003) 241–250.
- [6] D. Doğan, H. Türkdemir, Electrochemical oxidation of textile dye indigo, *J. Chem. Technol. Biotechnol.*, 80 (2005) 916–923.
- [7] L. Gui, J. Peng, P. Li, R. Peng, P. Yu, Y. Luo, Electrochemical degradation of dye on TiO<sub>2</sub> nanotube array constructed anode, *Chemosphere*, 235 (2019) 1189–1196.
- [8] T.T.V. Tran, S.R. Kumar, S.J. Lue, Separation mechanisms of binary dye mixtures using a PVDF ultrafiltration membrane: Donnan effect and intermolecular interaction, *J. Membr. Sci.*, 575 (2019) 38–49.
- [9] K.M. Majewska-Nowak, Application of ceramic membranes for the separation of dye particles, *Desalination*, 254 (2010) 185–191.
- [10] K. Szostak, M. Banach, Sorption and photocatalytic degradation of methylene blue on bentonite-ZnO-CuO nanocomposite, *J. Mol. Liq.*, 286 (2019) 110859, doi: 10.1016/j.molliq.2019.04.136.
- [11] D. Ayodhya, G. Veerabhadram, A review on recent advances in photodegradation of dyes using doped and heterojunction based semiconductor metal sulfide nanostructures for environmental protection, *Mater. Today Energy*, 9 (2018) 83–113.
- [12] J.M.S. Oliveira, M.R. de Lima e Silva, C.G. Issa, J.J. Corbi, M.H.R.Z. Damianovic, E. Foresti, Intermittent aeration strategy for azo dye biodegradation: a suitable alternative to conventional biological treatments?, *J. Hazard. Mater.*, 385 (2020) 121558, doi: 10.1016/j.jhazmat.2019.121558.
- [13] M.M. Martorell, H.F. Pajot, L.I.C.d. Figueroa, Biological degradation of Reactive Black 5 dye by yeast *Trichosporon akihoshidainum*, *J. Environ. Chem. Eng.*, 5 (2017) 5987–5993.
- [14] J. Yang, S. Yu, W. Chen, Y. Chen, Rhodamine B removal from aqueous solution by CT269DR resin: static and dynamic study, *Adsorpt. Sci. Technol.*, 37 (2019) 709–728.
- [15] L. Hu, C. Guang, Y. Liu, Z. Su, S. Gong, Y. Yao, Y. Wang, Adsorption behavior of dyes from an aqueous solution onto composite magnetic lignin adsorbent, *Chemosphere*, 246 (2020) 125757, doi: 10.1016/j.chemosphere.2019.125757.

- [16] J.N. Wekoye, W.C. Wanyonyi, P.T. Wangila, M.K. Tonui, Kinetic and equilibrium studies of Congo red dye adsorption on cabbage waste powder, *Environ. Chem. Ecotoxicol.*, 2 (2020) 24–31.
- [17] I. Anastopoulos, I. Pashalidis, A.G. Orfanos, I.D. Manariotis, T. Tatarchuk, L. Sellaoui, A. Bonilla-Petriciolet, A. Mittal, A. Núñez-Delgado, Removal of caffeine, nicotine and amoxicillin from (waste)waters by various adsorbents. A review, *J. Environ. Manage.*, 261 (2020) 110236, doi: 10.1016/j.jenvman.2020.110236.
- [18] V. Kumar, P. Saharan, A.K. Sharma, A. Umar, I. Kaushal, A. Mittal, Y. Al-Hadeethi, B. Rashad, Silver doped manganese oxide-carbon nanotube nanocomposite for enhanced dye-sequestration: isotherm studies and RSM modelling approach, *Ceram. Int.*, 46(8 Pt. A) (2020) 10309–10319.
- [19] A.K. Jain, V.K. Gupta, S. Jain, Suhas, Removal of chlorophenols using industrial wastes, *Environ. Sci. Technol.*, 38 (2004) 1195–1200.
- [20] V.K. Gupta, I. Ali, Removal of endosulfan and methoxychlor from water on carbon slurry, *Environ. Sci. Technol.*, 42 (2008) 766–770.
- [21] J. Mittal, V. Thakur, A. Mittal, Batch removal of hazardous azo dye Bismark Brown R using waste material hen feather, *Ecol. Eng.*, 60 (2013) 249–253.
- [22] S. Chen, Y. Huang, X. Han, Z. Wu, C. Lai, J. Wang, Q. Deng, Z. Zeng, S. Deng, Simultaneous and efficient removal of Cr(VI) and methyl orange on LDHs decorated porous carbons, *Chem. Eng. J.*, 352 (2018) 306–315.
- [23] L. Ai, M. Li, L. Li, Adsorption of methylene blue from aqueous solution with activated carbon/cobalt ferrite/alginate composite beads: kinetics, isotherms, and thermodynamics, *J. Chem. Eng. Data*, 56 (2011) 3475–3483.
- [24] N. Somsesta, V. Sricharoenchaikul, D. Aht-Ong, Adsorption removal of methylene blue onto activated carbon/cellulose biocomposite films: equilibrium and kinetic studies, *Mater. Chem. Phys.*, 240 (2020) 122221, doi: 10.1016/j.matchemphys.2019.122221.
- [25] H. Daraei, A. Mittal, Investigation of adsorption performance of activated carbon prepared from waste tire for the removal of methylene blue dye from wastewater, *Desal. Water Treat.*, 90 (2017) 294–298.
- [26] F. Dhaouadi, L. Sellaoui, G.L. Dotto, A. Bonilla-Petriciolet, A. Erto, A.B. Lamine, Adsorption of methylene blue on comminuted raw avocado seeds: Interpretation of the effect of salts via physical monolayer model, *J. Mol. Liq.*, 305 (2020) 112815, doi: 10.1016/j.molliq.2020.112815.
- [27] I. Anastopoulos, G.Z. Kyzas, Agricultural peels for dye adsorption: a review of recent literature, *J. Mol. Liq.*, 200 (2014) 381–389.
- [28] B. Huang, R. Zhao, H. Xu, J. Deng, W. Li, J. Wang, H. Yang, L. Zhang, Adsorption of methylene blue on bituminous coal: adsorption mechanism and molecular simulation, *ACS Omega*, 4 (2019) 14032–14039.
- [29] L.C.A. Oliveira, M. Gonçalves, D.Q.L. Oliveira, M.C. Guerreiro, L.R.G. Guilherme, R.M. Dallago, Solid waste from leather industry as adsorbent of organic dyes in aqueous-medium, *J. Hazard. Mater.*, 141 (2007) 344–347.
- [30] L. Chen, Y. Li, Q. Du, Z. Wang, Y. Xia, E. Yedinak, J. Lou, L. Ci, High performance agar/graphene oxide composite aerogel for methylene blue removal, *Carbohydr. Polym.*, 155 (2017) 345–353.
- [31] A.A. Adeyemo, I.O. Adeoye, O.S. Bello, Adsorption of dyes using different types of clay: a review, *Appl. Water Sci.*, 7 (2017) 543–568.
- [32] S. Rahmani, B. Zeynizadeh, S. Karami, Removal of cationic methylene blue dye using magnetic and anionic-cationic modified montmorillonite: kinetic, isotherm and thermodynamic studies, *Appl. Clay Sci.*, 184 (2020) 105391, doi: 10.1016/j.clay.2019.105391.
- [33] I. Anastopoulos, A. Mittal, M. Usman, J. Mittal, G. Yu, A. Núñez-Delgado, M. Kornaros, A review on halloysite-based adsorbents to remove pollutants in water and wastewater, *J. Mol. Liq.*, 269 (2018) 855–868.
- [34] G. Bauer, D. Ongari, D. Tiana, P. Gäumann, T. Rohrbach, G. Pareras, M. Tarik, B. Smit, M. Ranocchiari, Metal-organic frameworks as kinetic modulators for branched selectivity in hydroformylation, *Nat. Commun.*, 11 (2020) 1059, doi: 10.1038/s41467-020-14828-6.
- [35] M. Keshvardoostchokami, M. Majidi, A. Zamani, B. Liu, Adsorption of phenol on environmentally friendly Fe<sub>3</sub>O<sub>4</sub>/chitosan/zeolitic imidazolate framework-8 nanocomposite: optimization by experimental design methodology, *J. Mol. Liq.*, 323 (2021) 115064, doi: 10.1016/j.molliq.2020.115064.
- [36] D. Barpaga, V.T. Nguyen, B.K. Medasani, S. Chatterjee, B.P. McGrail, R.K. Motkuri, L.X. Dang, Insight into fluorocarbon adsorption in metal-organic frameworks via experiments and molecular simulations, *Sci. Rep.*, 9 (2019) 10289, doi: 10.1038/s41598-019-46269-7.
- [37] C. Arora, S. Soni, S. Sahu, J. Mittal, P. Kumar, P.K. Bajpai, Iron based metal organic framework for efficient removal of methylene blue dye from industrial waste, *J. Mol. Liq.*, 284 (2019) 343–352.
- [38] S. Soni, P.K. Bajpai, J. Mittal, C. Arora, Utilisation of cobalt doped iron based MOF for enhanced removal and recovery of methylene blue dye from waste water, *J. Mol. Liq.*, 314 (2020) 113642, doi: 10.1016/j.molliq.2020.113642.
- [39] Z. Cheng, J. Liao, B. He, F. Zhang, F. Zhang, X. Huang, L. Zhou, One-step fabrication of graphene oxide enhanced magnetic composite gel for highly efficient dye adsorption and catalysis, *ACS Sustainable Chem. Eng.*, 3 (2015) 1677–1685.
- [40] X. Zheng, H. Zheng, Y. Zhou, Y. Sun, R. Zhao, Y. Liu, S. Zhang, Enhanced adsorption of Orange G from aqueous solutions by quaternary ammonium group-rich magnetic nanoparticles, *Colloids Surf., A*, 580 (2019) 123746, doi: 10.1016/j.colsurfa.2019.123746.
- [41] S. Liu, C. Li, J. Yu, Q. Xiang, Improved visible-light photocatalytic activity of porous carbon self-doped ZnO nanosheet-assembled flowers, *CrystEngComm*, 13 (2011) 2533–2541.
- [42] D. Capková, M. Almáši, T. Kazda, O. Čech, N. Király, P. Čudek, A.S. Fedorková, V. Hornebecq, Metal-organic framework MIL-101(Fe)-NH<sub>2</sub> as an efficient host for sulphur storage in long-cycle Li-S batteries, *Electrochim. Acta*, 354 (2020) 136640, doi: 10.1016/j.electacta.2020.136640.
- [43] M. Almáši, V. Zelenák, P. Palotai, E. Beňová, A. Zelenáková, Metal-organic framework MIL-101(Fe)-NH<sub>2</sub> functionalized with different long-chain polyamines as drug delivery system, *Inorg. Chem. Commun.*, 93 (2018) 115–120.
- [44] F. Çiçek, D. Özer, A. Özer, A. Özer, Low cost removal of reactive dyes using wheat bran, *J. Hazard. Mater.*, 146 (2007) 408–416.
- [45] L. Zhang, Z. Cheng, X. Guo, X. Jiang, R. Liu, Process optimization, kinetics and equilibrium of orange G and acid orange 7 adsorptions onto chitosan/surfactant, *J. Mol. Liq.*, 197 (2014) 353–367.
- [46] T. Wang, P. Zhao, N. Lu, H. Chen, C. Zhang, X. Hou, Facile fabrication of Fe<sub>3</sub>O<sub>4</sub>/MIL-101(Cr) for effective removal of acid red 1 and orange G from aqueous solution, *Chem. Eng. J.*, 295 (2016) 403–413.
- [47] M. Cai, J. Su, Y. Zhu, X. Wei, M. Jin, H. Zhang, C. Dong, Z. Wei, Decolorization of azo dyes Orange G using hydrodynamic cavitation coupled with heterogeneous Fenton process, *Ultrason. Sonochem.*, 28 (2016) 302–310.
- [48] M. Ghaedi, A. Hassanzadeh, S. Kokhdan, Multiwalled carbon nanotubes as adsorbents for the kinetic and equilibrium study of the removal of alizarin red s and morin, *J. Chem. Eng. Data*, 56 (2011) 2511–2520.
- [49] Y.S. Ho, Selection of optimum sorption isotherm, *Carbon*, 42 (2004) 2115–2116.
- [50] N.T. Hai, S.J. You, H.P. Chao, Thermodynamic parameters of cadmium adsorption onto orange peel calculated from various methods: a comparison study, *J. Environ. Chem. Eng.*, 4 (2016) 2671–2682.
- [51] O. Pezoti, A.L. Cazetta, K.C. Bedin, L.S. Souza, A.C. Martins, T.L. Silva, O.O. Santos Júnior, J.V. Visentainer, V.C. Almeida, NaOH-activated carbon of high surface area produced from guava seeds as a high-efficiency adsorbent for amoxicillin

- removal: kinetic, isotherm and thermodynamic studies, *Chem. Eng. J.*, 288 (2016) 778–788.
- [52] S. Norouzi, M. Heidari, V. Alipour, O. Rahmadian, M. Fazlzadeh, F. Mohammadi-moghadam, H. Nourmoradi, B. Goudarzi, K. Dindarloo, Preparation, characterization and Cr(VI) adsorption evaluation of NaOH-activated carbon produced from Date Press Cake; an agro-industrial waste, *Bioresour. Technol.*, 258 (2018) 48–56.
- [53] P.S. Ghosal, A.K. Gupta, Determination of thermodynamic parameters from Langmuir isotherm constant-revisited, *J. Mol. Liq.*, 225 (2017) 137–146.
- [54] F. An, R. Wu, M. Li, T. Hu, J. Gao, Z. Yuan, Adsorption of heavy metal ions by iminodiacetic acid functionalized D301 resin: kinetics, isotherms and thermodynamics, *React. Funct. Polym.*, 118 (2017) 42–50.
- [55] E.C. Lima, A. Hosseini-Bandegharai, J.C. Moreno-Piraján, I. Anastopoulos, A critical review of the estimation of the thermodynamic parameters on adsorption equilibria, wrong use of equilibrium constant in the Van't Hoof equation for calculation of thermodynamic parameters of adsorption, *J. Mol. Liq.*, 273 (2019) 425–434.
- [56] I. Anastopoulos, G.Z. Kyzas, Are the thermodynamic parameters correctly estimated in liquid-phase adsorption phenomena?, *J. Mol. Liq.*, 218 (2016) 174–185.
- [57] M.J. Ahmed, Application of agricultural based activated carbons by microwave and conventional activations for basic dye adsorption: review, *J. Environ. Chem. Eng.*, 4 (2016) 89–99.
- [58] F. Wu, R. Tseng, R. Juang, Characteristics of Elovich equation used for the analysis of adsorption kinetics in dye-chitosan systems, *Chem. Eng. J.*, 150 (2009) 366–373.
- [59] F. Zhu, S. Ma, T. Liu, X. Deng, Green synthesis of nano zero-valent iron/Cu by green tea to remove hexavalent chromium from groundwater, *J. Cleaner Prod.*, 174 (2018) 184–190.
- [60] A.A. Atia, A.M. Donia, W.A. Al-Amrani, Adsorption/desorption behavior of acid orange 10 on magnetic silica modified with amine groups, *Chem. Eng. J.*, 150 (2009) 55–62.
- [61] Z.A. Sutirman, M.M. Sanagi, K.J. Abd Karim, A. Abu Naim, W.A. Wan Ibrahim, Enhanced removal of Orange G from aqueous solutions by modified chitosan beads: performance and mechanism, *Int. J. Biol. Macromol.*, 133 (2019) 1260–1267.
- [62] M.A. Salam, S.A. Kosa, A.A. Al-Beladi, Application of nanoclay for the adsorptive removal of Orange G dye from aqueous solution, *J. Mol. Liq.*, 241 (2017) 469–477.
- [63] L. Doumic, G. Salierno, M. Cassanello, P. Haure, M. Ayude, Efficient removal of Orange G using Prussian Blue nanoparticles supported over alumina, *Catal. Today*, 240 (2015) 67–72.